

Residual Stress States in Microstructurally Graded PBF–LB/M Austenitic Steel Components

Nico Möller,* Florian Loebich, Thomas Wegener, Julia Richter, Jens Gibmeier, and Thomas Niendorf

Laser-based powder bed fusion of metals (PBF–LB/M) represents a manufacturing technique enabling the production of application-adapted components. The process is influenced by multiple factors that interact during fabrication. Eventually, these lead to complex cooling conditions, resulting in microstructures strongly affecting the mechanical properties. Understanding the process-microstructure-property relationships is therefore crucial. The present study investigates microstructurally graded components made of austenitic steel 316L. Focus is on microstructural differences and residual stress evolution. Components are manufactured by utilizing a dual-laser system, consisting of a 400 W Gaussian and a 1 kW top-hat laser. Strengthening is strongly promoted by sub-structures, i.e. specific dislocation arrangements, decorated with chromium and molybdenum segregations. As a result, PBF–LB/M processed 316L demonstrates superior quasi-static properties compared to conventionally manufactured 316L. Differing cooling rates prevailing in areas processed either with the 400 W or the 1 kW laser significantly influence the substructure size, eventually resulting in distinctive strength and hardness. The incremental hole drilling method, considering local crystallographic orientation for data evaluation, was used to analyze changes in the residual stress distribution at different specimen-handling stages and lateral residual stress depth distributions. Results obtained pinpoint a pronounced in-depth gradient and a rather homogeneous lateral residual stress depth distribution.

1. Introduction

Powder bed-based additive manufacturing (AM) techniques offer a unique range of possibilities for tailoring application-oriented properties in structures and components. The tool-free near-net-shape production of complex geometries is directly derived from a 3D computer-aided design file.^[1] The most common AM processing technique, i.e., laser-based powder bed fusion of metals (PBF–LB/M), uses a laser beam as a source to transfer focused energy into the metal powder bed. 3D components are formed through the localized melting of the part geometry layer by layer in an inert atmosphere.^[2] In the case of PBF–LB/M, a variety of process parameters, such as laser scanning velocity, laser power, beam profile, hatch distance, and layer thickness, lead to a complex interplay resulting in microstructures and eventually mechanical features being different compared to conventionally processed counterparts.^[3]


Besides a very good corrosion resistance, the austenitic stainless steel AISI 316L is known for good weldability due to its low carbon content of 0.03 wt%. This character-

istic makes it perfectly suitable for processing via PBF–LB/M.^[4] A wide range of process parameter combinations, resulting in parts with a high density, enables structural integrity within a large process window.^[5–8]

Within this process window, multiple factors affect the thermal cooling history and, hence, the microstructural properties of the built parts. Process-inherent rapid cooling and heating rates as well as high thermal gradients in the melt pool lead to an epitaxial, columnar grain growth along the build direction (BD). This is caused by the directed heat flux dissipating from the liquid material through the solidified material into the build plate.^[9] High cooling rates lead typically to a microstructure with relatively fine grains, which are in the range of 50–100 µm for PBF–LB/M processed 316L.^[6,10,11] Increasing the volume energy density enhances grain growth and fosters a preferred <001> crystallographic texture with respect to cooling direction in face-centered cubic (FCC) materials. Furthermore, Chandra et al.^[12] proposed grain size and morphology modification of 316L by varying the powder size. It is seen that finer powder triggers the formation of coarse grains, whereas fine grains are obtained

N. Möller, T. Wegener, J. Richter, T. Niendorf
Institute of Materials Engineering – Metallic Materials
University of Kassel
Mönchebergstraße 3, 34125 Kassel, Germany
E-mail: n.moeller@uni-kassel.de

F. Loebich, J. Gibmeier
Institute for Applied Materials (IAM-WK)
Karlsruhe Institute of Technology (KIT)
Engelbert-Arnold-Straße 4, 76131 Karlsruhe, Germany

 The ORCID identification number(s) for the author(s) of this article can be found under <https://doi.org/10.1002/adem.202500412>.

© 2025 The Author(s). Advanced Engineering Materials published by Wiley-VCH GmbH. This is an open access article under the terms of the Creative Commons Attribution License, which permits use, distribution and reproduction in any medium, provided the original work is properly cited.

DOI: 10.1002/adem.202500412

by coarse powder. In addition to microstructure features on the grain level, substructures, i.e., low-angle grain boundaries smaller than 1 μm , have been reported. These substructures are forming a cellular network. Zhong et al.^[11] determined the size of such cellular network structures to be in the range of 0.5–1 μm . The substructure size can serve as a parameter to assess the process-inherent cooling rates following the approach of dendrite arm spacing, for example, in refs. [13–15]. Higher cooling rates result in a finer dendrite arm spacing and vice versa. Elemental segregation of molybdenum (Mo) and chromium (Cr) is detectable at these substructures. Previous studies attribute the formation of the substructures to the phenomenon of constitutional undercooling and dendrite formation. Mo and Cr are characterized by comparably high melting points of 2623 °C and 1875 °C, respectively.^[16,17] In the case of 316L, the lower melting point elements, i.e., iron (Fe) and nickel (Ni), are primary solidifying at the solid/liquid interface in the melt pool, hence locally enriching the liquid with Mo and Cr.^[18,19] Due to these solute elements, the liquidus temperature is locally reduced in comparison to the remaining melt and increases with a higher distance from the liquid/solid interface. If the actual melt pool temperature is below the solidification temperature, the melt is locally constitutionally undercooled, eventually promoting cellular and dendritic growth.^[20,21] Differences regarding the morphology of subgrain structures were categorized by Yang et al.^[22] as elongated cellular, strip, or hexagonal, which are formed due to different Marangoni convection flows in the melt pool. Besides the elemental segregation, the formation of nano-scaled oxides can be found within the boundaries of the substructures.^[11,23] Wang et al.^[24] point at dislocation accumulation at the cell boundaries rationalized by a pinning mechanism. Both substructures and nano-scaled oxides can act as obstacles to trap dislocations.^[11] Still, in literature, the phenomenon of substructure formation is discussed controversially, as some authors also consider the substructures as a cellular dislocation network.^[25,26]

Generally, the formation of a high dislocation density in PBF–LB/M processed 316L is the result of the complex thermal history. Repetitive melting and solidification of several scan tracks, coupled with high-temperature gradients and high cooling rates, cause the formation of residual stress. Localized melting of a considerably small spot induces thermal material expansion in the surrounding heat-affected zone, eventually leading to temporary compressive stresses. Due to rapid cooling, shrinking of the solidifying material, which is bound to formerly thermally expanded zones, occurs.^[27–30] As a consequence, thermal cycling in PBF–LB/M processes leads to a complex residual stress state within an as-built component, and eventually, structural defects such as cracks, delamination, and warping can arise.^[31] Moreover, stress fields affect the mechanical properties due to the superposition of the externally applied mechanical stress, which becomes especially important under fatigue loading.^[32,33]

Due to the possibility of tailoring microstructural features, the correlating mechanical properties can be adapted in dependence of the application. As in the case of PBF–LB/M manufactured 316L, superior mechanical properties can be achieved compared to conventionally produced parts (i.e., wrought and cast 316L). A significant enhancement by a factor of 2–3 in yield strength is

reported for PBF–LB/M produced parts compared to wrought and cast 316L, which is in the range of 200–345 MPa.^[7,8,34–36] Nevertheless, high elongation to fracture (EF) of up to 52.5% for PBF–LB/M processed 316L, as reported by several authors,^[33,37] can be maintained. Hardness is found to be in the range of 220–245 HV for both wrought and PBF–LB/M conditions of 316L,^[6–8,35,38] while cast 316L, as investigated by Bartolomeu et al.^[35] exhibits an average hardness of 170 HV. The high yield strength in PBF–LB/M processed 316L can be attributed to the unique existence of the substructures in combination with a high dislocation density and nano-scaled oxides.^[25] Generally, plastic deformation is driven by the movement of dislocations.^[39,40] Planar slip, as it occurs in 316L, is hindered by the ascribed microstructural features.^[41] On a macro-scale, grain boundary strengthening, following the Hall–Petch relation, increases the yield strength due to smaller grains in PBF–LB/M 316L compared to the cast 316L. Furthermore, dislocation strengthening, as mentioned by Zhou et al.^[25] seems to be the dominant strengthening mechanism in AM-processed 316L, followed by solid solution strengthening attributed to the alloying elements. The cellular substructures act as obstacles for dislocation movement, which leads to dislocation accumulation and hence fosters dislocation–dislocation interactions. Additionally, nano-scaled oxides generate local stress fields and, thus, further enhance pinning of dislocations.^[24,25]

Besides the strengthening mechanisms detailed so far, crystallographic texture is an important microstructural factor determining the degree of anisotropy regarding monotonic mechanical properties. Kumar et al.^[42] reported the impact of crystallographic texture, adjusted via the hatch scan rotation, on the deformation mechanism in uniaxial compression testing. Thereby, a (001) and (110) crystallographic texture promotes slip and twin formation, whereas an only (001)-textured specimen deforms only via slip. Loading along a (001)-textured specimen of PBF–LB/M processed 316L reveals a reduction in Young's modulus (YM) by a factor of two compared to a rather isotropic microstructure.^[43] Moreover, Stinville et al.^[44] reported that not only the YM is the lowest in the (001)-direction, but also the strength, as indicated by the hardness, drops to a minimum.

According to these observations, microstructural gradation of PBF–LB/M processed 316L, as proposed by Niendorf et al.^[38] can be achieved through process design, in part by utilizing a dual-laser system. Such a laser system, being equipped with two lasers featuring different maximum nominal laser powers of 1 kW and 400 W as well as different beam shapes (i.e., a Gaussian profile and a top-hat profile for the 400 W and 1 kW laser, respectively), eventually leads to the evolution of locally differing microstructures within the same part: a coarse-grained, columnar, and strong (001)-textured microstructure upon utilization of the 1 kW laser and a fine-grained, equiaxed, and almost isotropic microstructure upon using the 400 W laser. The locally differing microstructures are also distinguishable with respect to their mechanical properties in uniaxial tensile tests. Here, locally different specimen zones can be identified by their varying local strain evolution using digital image correlation (DIC), with the coarse and textured microstructure exhibiting premature strain accumulation compared to the fine-grained zone.^[45]

Based on the studies of Niendorf et al.^[38,45] Brenne et al.^[10] processed microstructurally graded 316L cuboids via PBF–LB/M

by exploiting the approach detailed before. Compact tension (CT) specimens were wire-cut and investigated in terms of crack growth rates. The authors showed that a crack can be arrested when the crack tip enters a coarse-grained specimen region, if the crack growth direction is perpendicular to the grain's long axis. Furthermore, crack growth rates could be reduced due to higher crack deflection in the coarse-grained 1 kW built area compared to the fine-grained 400 W area.^[33] However, only bulk cuboids were manufactured and studied, which fails to match the light-weight potentials of PBF–LB/M. Furthermore, the impact of residual stress fields in the microstructurally graded specimens remained unexplored.

Microstructural gradation by means of tailoring crystallographic texture and grain size properties through adaption of process parameters of PBF–LB/M can serve as a reasonable manufacturing technique to design load-optimized components. Therefore, the present study aims to provide a comprehensive understanding of microstructurally graded PBF–LB/M 316L specimens, built with a dual-laser system by applying comparably low- and high-volume energy densities, including suitable laser power, hatch distance, and laser scanning velocity. Within the objective to achieve specimens being characterized by high relative density, PBF–LB/M process parameters are adapted to yield in strongly crystallographic textured and coarse-grained specimen areas, compared to weak-textured and more equiaxed areas inside the same specimen. The focus is on the process–microstructure–property relationships, with particular focus on wall-like components. Wall-like structures are chosen to assess application-oriented near-net shape components, to maintain the process-inherent benefits of PBF–LB/M and to consider constraints that are more appropriate for a wall-like component. Here, the combination of vast differences in process parameters, eventually resulting in microstructurally and quasi-statically distinguishable specimen areas, promotes the evolution of a highly complex residual stress field. Examination of microstructural features is conducted using scanning electron microscopy (SEM), electron backscatter diffraction (EBSD), energy-dispersive X-ray spectroscopy (EDS), as well as X-ray diffraction (XRD). Moreover, the mechanical properties are evaluated by uniaxial tensile tests and Vickers hardness mappings. To uncover residual stress distribution states resulting from the PBF–LB/M process, the incremental hole-drilling method is applied. Accordingly, the presented study serves as a framework for ongoing studies, focusing on the interplay of residual stress fields and the fatigue crack growth behavior within microstructurally graded specimens.

2. Experimental Section

2.1. Material and Specimen Preparation

For the investigations presented, AISI 316L stainless steel powder obtained from SLM Solutions Group AG, Germany, was used for the fabrication of specimens via PBF–LB/M. The chemical composition of the virgin powder, provided by the powder supplier, is presented in **Table 1**. According to particle size distribution analysis conducted by the supplier, d_{10} , d_{50} , and d_{90} values of the spherical powder particles were determined as 19.39, 32.24, and 53.63 μm , respectively.

The fabrication of specimens was conducted on a SLM 280^{HL} machine (SLM Solutions Group AG, Germany), equipped with a dual-laser system consisting of lasers with a nominal maximum power of 400 W and 1 kW, respectively. The 1 kW laser is operated with a top-hat-shaped intensity profile, whereas the 400 W laser offers a Gaussian intensity profile. The 1 kW top-hat laser is characterized by a beam diameter of 1 mm according to machine supplier, whereas the 400 W Gaussian laser is characterized by a diameter of 80 μm . Based on preliminary parameter studies focusing on the relative density of the parts as well as microstructural evolution (not detailed for the sake of brevity), different process parameters were chosen depending on the applied laser (cf. **Figure 1**). The 1 kW laser was set to 900 W with a scanning velocity of 800 mm s^{-1} and a hatch distance of 0.05 mm. The 400 W laser instead operated at 325 W, a scanning velocity of 700 mm s^{-1} , and a hatch distance of 0.12 mm. Independent of the applied laser the layer thickness was always set to 0.05 mm. The hatch scan was rotated at an angle of 90° layer by layer, with a 45° starting angle with respect to the normal direction (ND) (cf. **Figure 1**). Rectangular tube profiles (cf. **Figure 1**) with a wall thickness of 4 mm and dimensions of 40 mm in length, width, and height were built on a base plate featuring a size of 220 × 220 mm^2 in argon atmosphere. The tube profile is divided into two equal sections in which either the 1 kW laser or the 400 W laser is applied; hence the terminology “400 W” and “1 kW” area, respectively, will be used in the remainder of this work to capture the distinctive microstructural texture and grain size within the specimen. Furthermore, the side surfaces of the tube profile solely built by the 400 W or 1 kW laser are defined as areas A and B. Microstructurally graded specimens, i.e., specimens of the tube with an interface of 400 W and 1 kW, are referred to as area C. To ensure proper bonding at the interface, in which the applied laser switches, an overlap of 200 μm was chosen. To reduce the surface roughness, specimen areas processed using the 1 kW laser, are covered by a thin shell of 200 μm of material processed by the 400 W laser.

Table 1. Chemical composition in weight percent (wt%) of AISI 316L powder provided by the powder supplier and standard composition details.^[76,77]

	wt%	C	Cr	Fe	Mn	Mo	Ni	P	S	Si	N	O
	Actual	0.02	17.75	Bal.	0.82	2.38	12.6	0.010	0.01	0.69	0.09	0.02
ASTM A276	Min.	–	16.0	Bal.	–	2.0	10.0	–	–	–	–	–
	Max.	0.03	18.0	Bal.	2.0	3.0	14.0	0.045	0.03	1.0	–	–
DIN EN 10088	Min.	–	16.5	Bal.	–	2.0	10.0	–	–	–	–	–
	Max.	0.03	18.5	Bal.	2.0	2.5	13.0	0.045	0.03	1.0	0.10	–

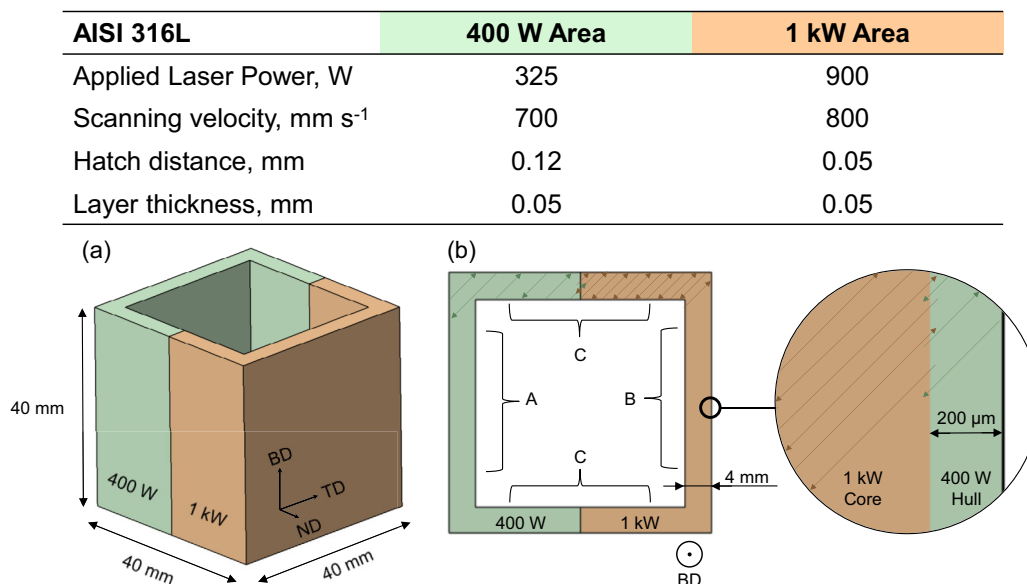


Figure 1. Process parameters and build geometry of PFB-LB/M manufactured microstructural graded 316L specimens in a) isometric view and b) top view schematically highlighting the scan pattern.

2.2. Microstructure Characterization

For microstructural characterization, graded specimens were cut within the interface of area C. In order to exclude surface effects, stepwise mechanical grinding down to the core of the depicted specimens was conducted. Surface preparation to a grit size of 1 μm using SiC paper was followed by vibro-polishing using oxide polishing suspension for at least 8 h. Etching of depicted polished specimens was applied to enhance the visibility of the substructures. Immersion in a reagent containing 3HCl:1HNO₃:4H₂O for a minimum of 45 s was found to be suitable for providing satisfactory results. After the metallographic treatment, all specimens were ultrasonic cleaned in ethanol for 5 min, to remove any residuals from the surface.

The microstructural analysis was conducted on a Zeiss ULTRA GEMINI SEM (Carl Zeiss AG, Germany) equipped with an EBSD unit and an EDS detector. The acceleration voltage was set to 20 kV for both EBSD and EDS analysis. The EBSD measurements were performed at magnifications of either 32 \times with a step size of 4 μm for an overview or 2000 \times with a step size of 25 nm for a more detailed observation. A finer step size of 12 nm was chosen for the EDS mapping at a magnification of 2000 \times . Grain statistics were calculated with the software TSL OIM Analysis (Version 7.3.0) by EDAX Inc, USA. Investigation of the substructures to assess the dendrite arm spacing was carried out with the software ImageJ (Version 1.54 g) developed by Wayne Rasband et al.^[46]

2.3. Texture Analysis

To determine the integral crystallographic texture, complementary to local texture analyses by EBSD, XRD using a 4-circle diffractometer of type Seifert PTS and Fe-filtered Co-K α -radiation was applied. On the primary side, a pinhole collimator with a

nominal diameter of \varnothing 1 mm was used. On the secondary side of the beam path, a 4 mm slit was used in front of the scintillation counter. The specimens were aligned with the outside surface of the specimen along the ND and rotated along ψ from 0° to 70° and along ϕ from -170° to 170° with a step size of 5°. By this means incomplete pole figures for the {200}-, {220}-, {311}-, and {222}- planes were determined and from these pole figures the orientation distribution functions (ODF) were calculated using the MATLAB-toolbox MTEX.^[47] For visualization purposes, the $\phi_2 = 45^\circ$ sections through the ODFs were used (Bunge notation).

Depth profiles of the crystallographic texture were determined for both the 400 W area and the 1 kW area using support points in the depths of 20, 100, 200, 400, 600, 800, and 1000 μm defined from the outside surface. For each step, the material was removed using electropolishing and the texture analysis was carried out on the newly generated surface. To determine the crystallographic texture in the center of the specimen, the material was removed via grinding with subsequent polishing of the surface of about 100 μm , so in total a layer of 2 mm was removed to reach the mid-layer.

2.4. Mechanical Properties

Uniaxial tensile tests for the evaluation of quasi-static properties were carried out on a screw-driven MTS Criterion load frame with a maximum loading capability of 20 kN using a constant crosshead speed of 2 mm min⁻¹. A MTS miniature extensometer with a gauge length of 5 mm and 30% strain limit was applied on the side surface of dog-bone-shaped miniature tensile specimens which were cut via electro-discharge machining (EDM) directly out of area A and B (cf. Figure 2). Beyond the extensometer strain limit, nominal stress-strain diagrams were plotted based on the load and displacement signals as well as the gauge section

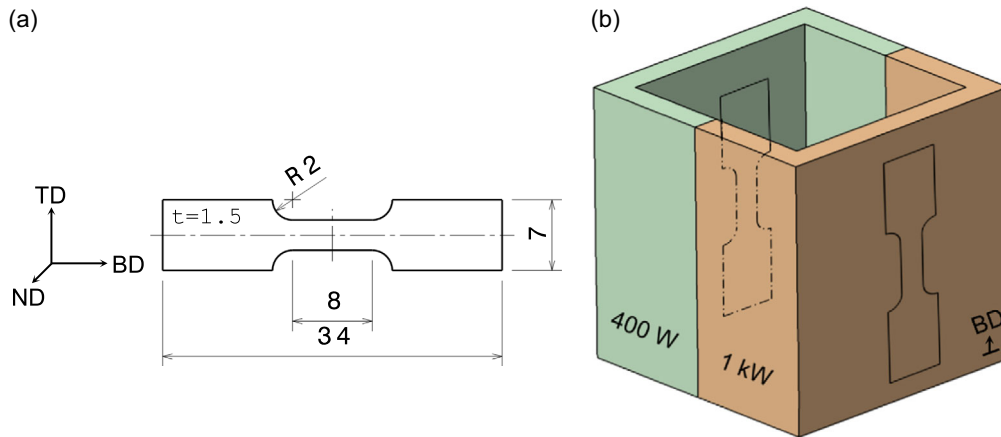


Figure 2. Specimen geometry used for a) tensile tests including b) their initial orientation in the PBF-LB/M build geometry.

dimensions of the specimens as given in Figure 2. The direction of the applied load was alongside BD. The surfaces of the dog-bone-shaped miniature specimens were mechanically ground down to a grit size of $15\ \mu\text{m}$ prior to tensile testing.

To reveal a gradient in microhardness, a Vickers hardness (HV) mapping was performed on a mechanically polished specimen. The mapping was conducted in the transverse direction-normal direction plane (TD-ND plane) (cf. Figure 1) normal to BD within an area of $3.8 \times 8\ \text{mm}^2$, covering the interface of the 400 W and 1 kW area. A distance of $200\ \mu\text{m}$ in *x*- and *y*-direction between adjacent measuring points resulted in a grid of 779 evaluable indents. A Zwick Roell DuraScan 70 G5 fully automated hardness testing machine equipped with a Vickers indenter, applying a maximum load of $0.49\ \text{N}$ (HV 0.05) at a dwell time of 10 s on each measurement point, was used for performing the indentation mapping.

2.5. Residual Stress Analysis

The local macroscopic residual stress depth profiles were analyzed using the incremental hole drilling method according to ASTM E837-20.^[48] For drilling, a TiN-coated end mill with a nominal diameter of $\varnothing\ 1.6\ \text{mm}$ and an RS200 air turbine (Vishay Measurements Group) were used. The strain relaxation after each increment was recorded using a strain gauge rosette of type CEA-06-062UM-120 (Micro-Measurements), which is equivalent to type B in ASTM E837-20. The strain gauge rosette at location 0° was aligned with BD and at location 90° with TD. The actual hole diameter was determined after drilling the last increment. The stress measurement was done on specimens in the as-built state and, therefore, without removal of the 400 W shell on the 1 kW area. For evaluation, the strain relaxation curves were conditioned using damped cubic spline functions. For stress calculation, the differential approach was applied.^[49] However, to account for the elastic anisotropy due to crystallographic texture, the evaluation approach proposed in ref. [50] was applied using case-specific calibration functions. For the calculation of these calibration functions, a finite-element (FE) model as described in refs. [51,52], consisting of 68 060 elements of type C3D8R, and a calibration stress value of $200\ \text{MPa}$ in TD- or BD direction

were applied. Unlike in refs. [50,51], in the present work, a depth gradient in terms of the crystallographic texture prevails, eventually affecting the stiffness tensor. Thus, the elastic constants are depth dependent. Therefore, the stiffness tensor based on the determined crystallographic texture was calculated according to the Hill criterion using the MATLAB-toolbox MTEX^[47] and the single crystal data $C_{11} = 206\ \text{GPa}$, $C_{12} = 133\ \text{GPa}$, and $C_{44} = 119\ \text{GPa}$ ^[53] for all texture measurement depths. These values were subsequently assigned to each depth layer in the FE model. Here, the stiffness tensor was linearly interpolated between two texture measurement depths.

In order to gain an insight into the effect of specimen handling on the residual stress distribution, the residual stress depth profiles were analyzed on a specimen still attached to the base plate, a specimen removed from the base plate via wire-EDM and a specimen removed from the base plate and cut open using a diamond wire saw. For each of those stages the incremental hole drilling method was applied in the center of the 400 W and the 1 kW areas A and B (cf. Figure 9). To determine the lateral residual stress distribution across the areas, the residual stress depth profiles were determined at four additional measurement points with an $\approx 10\ \text{mm}$ distance from the edges of the cut open state, for both the 400 W and the 1 kW area, respectively (cf. Figure 10).

3. Results

3.1. Microstructure and Crystallographic Texture

Figure 3 presents the results of microstructural analysis in form of representative EBSD inverse pole figure (IPF) maps plotted with respect to BD for a graded specimen of area C (cf. section 2) including both the 400 W and the 1 kW area, respectively. The front side view in Figure 3a reveals a sharp microstructural gradient with relatively fine and equiaxed grains in the 400 W area on the left side of the EBSD micrograph being characterized by a sickle-shaped grain structure. In contrast, coarse and columnar grains being elongated alongside BD are visible on the right side within the 1 kW area. Moreover, mixed stray grain morphologies are seen in a narrow transition zone of $\approx 200\ \mu\text{m}$ in between the

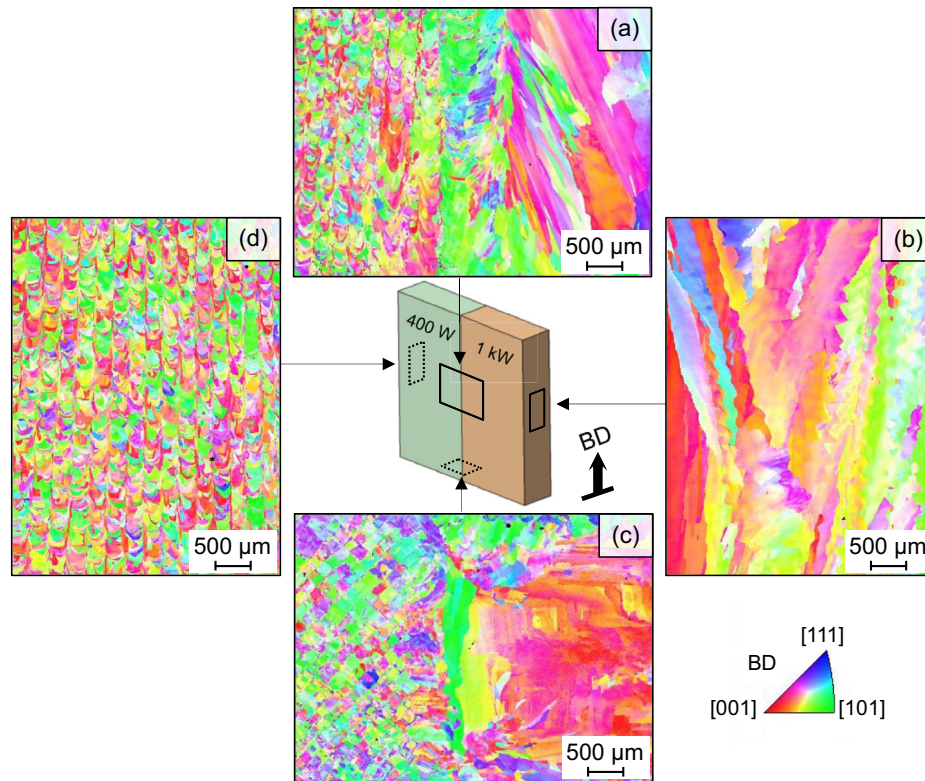


Figure 3. EBSD IPF maps of microstructurally graded specimens: a) front view, b) side view 1 kW area, c) downside view, and d) side view 400 W area. The grain orientations (see standard triangle) are plotted with respect to BD (vertical).

clearly distinguishable 400 W and 1 kW area. The side view of the 1 kW area in Figure 3b reveals relatively large, elongated grains with a zig-zag morphology along the grain boundaries. Figure 3c presents the downside view of the interface zone. A checkerboard pattern is seen in the 400 W area on the left side, which is aligned with the hatch scan rotation at an angle of 45° with respect to the front side. The 1 kW area shows larger grains with a preferred crystallographic $\langle 001 \rangle$ -orientation with respect to BD. Furthermore, these large, preferably $\langle 001 \rangle$ -oriented grains are surrounded by smaller grains differing in their crystallographic orientation pinpointing the onset of the 400 W shell layer. The 400 W area side view in Figure 3d appears similar to the 400 W front side view and hence emphasizes the contrast in grain size and morphology compared to the 1 kW area. The grain aspect ratio calculated from the front side view in Figure 1a is 0.36 and 0.16 for the 400 W and 1 kW area, respectively. Grain sizes are calculated by fitting an ellipse for each detected grain and determining the length of the major and minor axis, assuming that the major axis is aligned with BD and the minor axis with TD. In addition, the weighted average grain length with respect to the front side view reveals grain sizes of $1021 \times 174 \times 106 \mu\text{m}^3$ and $73 \times 26 \times 12 \mu\text{m}^3$ in length, width, and depth for the 1 kW area and for the 400 W area, respectively. The grain sizes of all three dimensions are evaluated based on the 2D EBSD measurements of the front, side, and top view of the 400 W and 1 kW area, respectively (cf. Figure 3). In some cases, the grains, especially those of the 1 kW area, exceed the

EBSD map in length. Hence, grain sizes and calculated aspect ratio have to be considered as a rough estimation.

Figure 4 presents results obtained for the crystallographic texture in different depths from the surface. In Figure 4a, the coordinate system for the XRD texture analysis in the center of areas A and B and the positions of selected standard orientations in ODF-sections at $\varphi_2 = 45^\circ$ are shown. Most important for this study are the cube texture at $\phi = 0^\circ$ and $\varphi_1 = 45^\circ$ as well as the Goss texture at $\phi = 90^\circ$ and $\varphi_1 = 90^\circ$. In Figure 4b, the ODF sections at $\varphi_2 = 45^\circ$ for the 400 W and the 1 kW area are shown for the center of the specimens at a depth of $\approx 2 \text{ mm}$. In the 400 W area, a primary Goss-type texture is determined. The 1 kW area instead shows a cube-type texture. The crystallographic texture in the 1 kW area is more pronounced as can be derived from the higher value of the m.r.d. (multiples of the random distribution) of the preferred orientation. The evolution in the crystallographic texture with increasing depth can be seen in Figure 4c. There, the ODF-sections at $\varphi_2 = 45^\circ$ are shown as an example for the depth values of 100, 400, and 1000 μm for the 400 W area. In the direct vicinity of the surface, i.e., at a depth of about 100 μm , no preferred crystallographic orientation is determined. This is also the case at a depth of about 200 μm . From a depth of about 400 μm on, a primary rotated Goss-like texture is present in the 400 W area being rotated from the ideal Goss texture by around 25° . With increasing depth, this misorientation decreases. At a depth of about 1000 μm , the primary crystallographic orientation is an ideal Goss texture. The

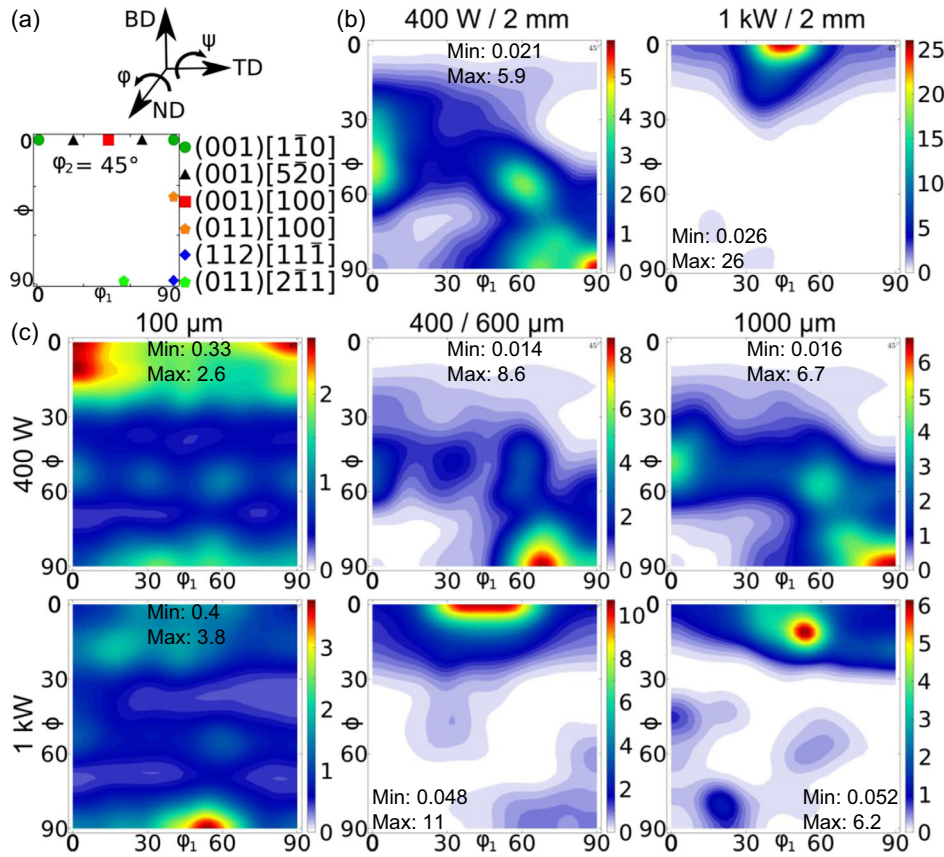


Figure 4. Results from XRD texture analysis: a) Coordinate system for texture analysis and positions of depicted standard orientations in ODF-sections at $\phi_2 = 45^\circ$; b) ODF-sections at $\phi_2 = 45^\circ$ for 400 W and 1 kW in 2 mm depth; c) ODF-sections at $\phi_2 = 45^\circ$ for 400 W and 1 kW in 100 μm , 400 μm (400 W) and 600 μm (1 kW) and 1000 μm depth.

characteristic of the crystallographic texture remains relatively constant from about 400 μm up to a depth of ≈ 2 mm.

In the 1 kW area near the surface, again no obvious preferred crystallographic orientation is determined. This absence of a pronounced crystallographic texture extends up to a depth between about 400 and 600 μm . At a depth of about 600 μm , a cube-like crystallographic texture is present as can be seen in Figure 4c, with the primary orientation being around the ideal cube texture. This continues to larger depths. Here a significant misorientation with respect to the ideal cube texture is obvious at a depth of about 1000 μm ; however, still a cube-like texture is present.

For a more detailed assessment of the microstructure with respect to substructure formation, EBSD IPF maps of the 400 W and 1 kW area, obtained on the front side view (cf. Figure 3) at higher magnification of 2000 \times , are shown in Figure 5a,b. In addition, Figure 5c,d depicts the corresponding secondary-electron (SE) contrast micrographs at the same spot. Melt pool boundaries, visible due to etching in Figure 5c,d, reveal a semi-elliptical formation. Grain growth exceeds the melt pool boundaries as can be deduced from a direct comparison of the IPF maps and the SEM images for both the 400 W and 1 kW area. Differing substructure morphologies, i.e., elongated cellular, strip, or hexagonal can be distinguished in both the 400 W area and in the 1 kW area (cf. Figure 5c,d). Transition of the

substructure morphology mainly occurs upon crossing melt pool boundaries, as can be clearly seen in the 400 W area (cf. Figure 5c). The strip cell morphology, which is elongated along BD, is apparent in the top left melt pool and sharply changes to hexagonal cell structures below. Nevertheless, altering cellular patterns can appear in some cases within a grain. This can be derived from direct comparison of Figure 5a,c in the 400 W area. The main difference between the 400 W and 1 kW area, considering the substructures, is rooted in different substructure sizes. In order to reveal the difference in subgrain size within one type of substructure morphology, honeycomb structures were examined by fitting an ellipse and calculating the diameter of the major and minor axes. Here, major axis diameters of 0.49 μm and 1.20 μm are found for the 400 W and 1 kW area, respectively.

To further analyze the cellular substructures, an EDS elemental mapping was conducted within the 1 kW area. The results are presented in Figure 6. For this EDS mapping, the major alloying elements of 316L, i.e., Fe, Cr, Ni, and Mo, were considered. As can be deduced from the results presented in Figure 6, the substructures precipitated in a Fe-rich matrix (Figure 6b) by element segregation of Cr and Mo (Figure 6c,e). Although Ni occurs slightly segregated in the substructures, it is more evenly distributed within the matrix than the other elements in the probed area (Figure 6d).

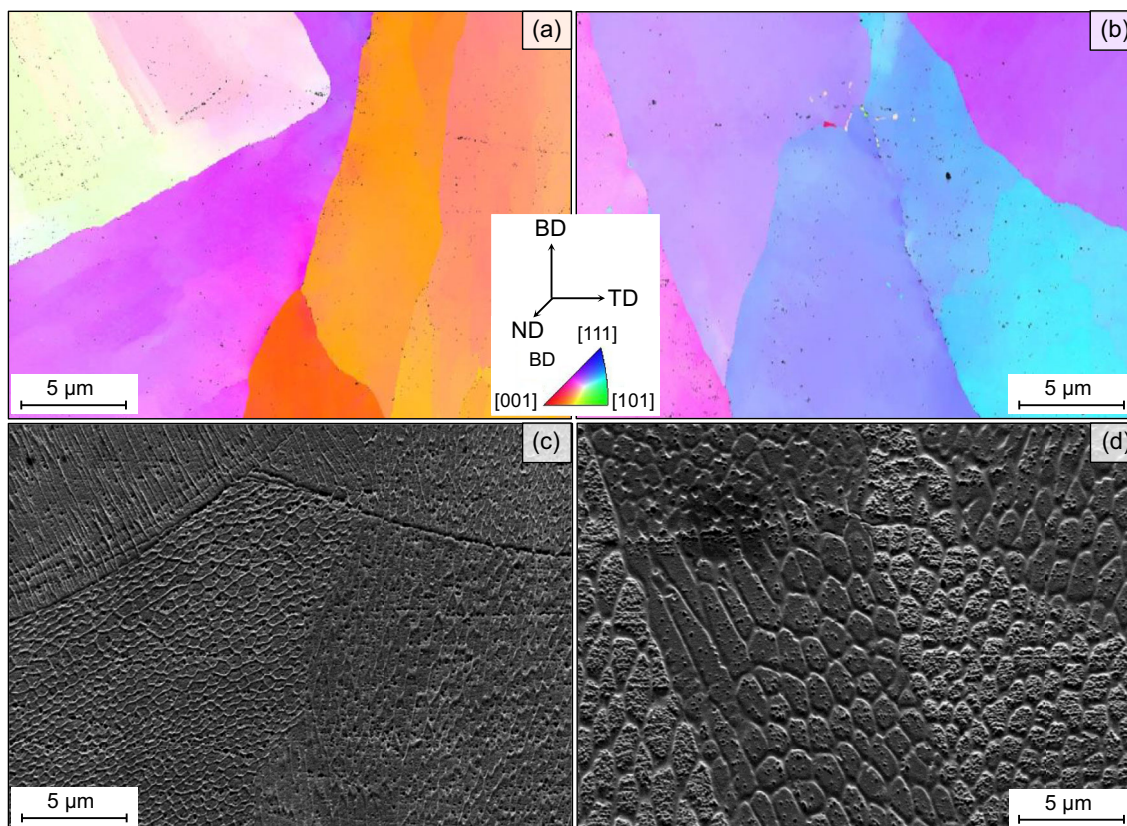


Figure 5. EBSD IPF maps of the front view: a) 400 W area and b) 1 kW area. The grain orientations (see standard triangle) are plotted with respect to BD (vertical); secondary electron SEM micrograph of cellular substructures at the same position as for the EBSD IPF maps presented in (a) and (b): c) 400 W area and d) 1 kW area.

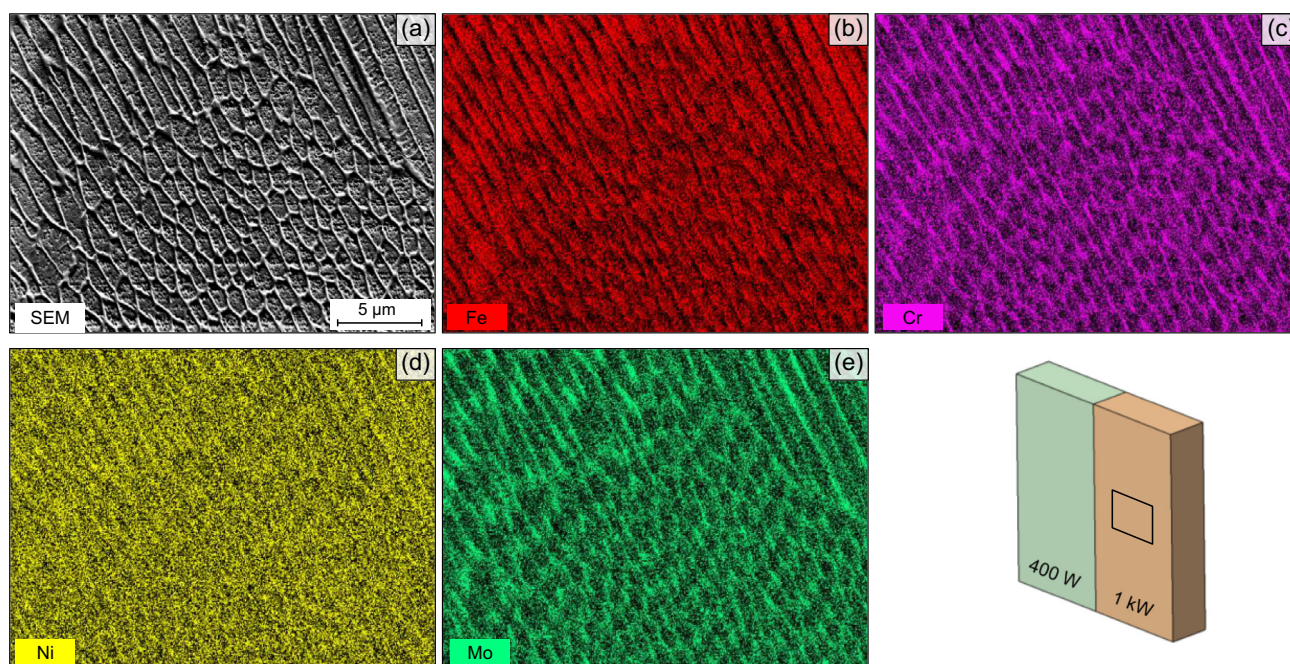


Figure 6. EDS elemental mapping of the substructures in the 1 kW area of a microstructurally graded 316L specimen manufactured by PBF–LB/M: a) SEM image, b) Fe, c) Cr, d) Ni, and e) Mo. The schematic of the specimen illustrates the position of the investigated area.

3.2. Mechanical Properties

The mechanical properties of the graded 316L specimens processed by PBF-LB/M were assessed by means of hardness measurements as well as tensile testing. **Figure 7** presents stress–strain curves obtained from tensile tests of non-graded specimens, which were cut from areas A and B (cf. section 2). The loading axis of the miniature specimens depicted in **Figure 7** corresponds to the BD. As can be seen, a total of three tests were conducted for each area. For the 400 W specimens, an ultimate tensile strength (UTS) of 618 ± 5 MPa is observed, compared to 542 ± 8 MPa for the 1 kW specimens. The macroscopic YM is evaluated as 145 ± 7 GPa for the specimens of the 1 kW area and 173 ± 7 GPa for the 400 W specimens. This difference in YM affects the analysis of the 0.2% yield offset ($R_{p0.2}$), which is 516 ± 5 MPa for the 400 W specimens and, hence, $\approx 22\%$ higher than the $R_{p0.2}$ of 424 ± 7 MPa for the 1 kW specimens. Additionally, the 400 W specimens exhibit a ratio of $R_{p0.2}$ to UTS of 0.83, indicating lower work hardening capability compared to the 1 kW specimens, the latter being characterized by a ratio of 0.78. The 1 kW specimens show a slightly higher uniform elongation (UE) of $33.7 \pm 5.3\%$ compared to $29.9 \pm 5.0\%$ for the 400 W specimens. However, despite this difference in UE, the 400 W specimens achieve a slightly superior EF of $63.9 \pm 2.1\%$, compared to $57.1 \pm 5.1\%$ for the 1 kW specimen. The most important characteristic values obtained from the tensile tests are summarized as average values in the table in **Figure 7**.

In addition to tensile testing, Vickers hardness measurements were carried out on a microstructurally graded specimen with a transition from the 400 W to the 1 kW area. In total, 779 individual measurements were conducted. The results obtained are shown in the hardness map in **Figure 8**. The position of each measurement point is represented by a white dot. An average surface hardness of 227 ± 14 HV0.05 is calculated for the

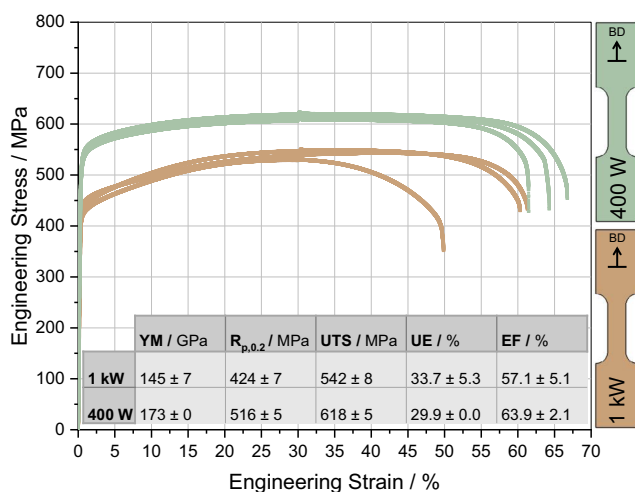


Figure 7. Tensile stress–strain curves for 400 W and 1 kW specimens. The inset on the right side schematically shows the specimen geometry used for tensile tests, where the loading direction is parallel to BD. The most important characteristic values obtained from the tensile tests are summarized as average values in the table at the lower part of the figure.

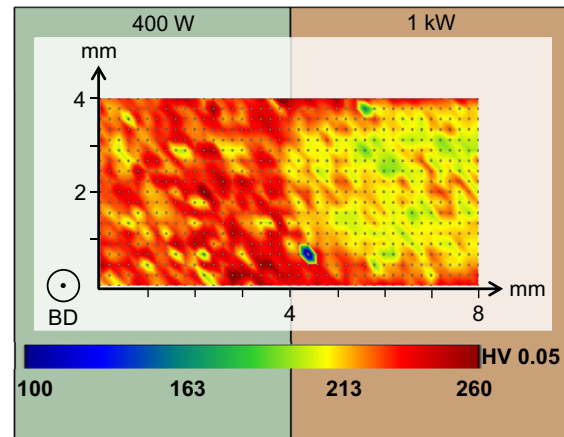


Figure 8. Vickers hardness (HV0.05) map showing the hardness distribution of the interface area C of a microstructurally graded 316L specimen manufactured by PBF-LB/M. White dots represent the position of each single measurement. The indentation direction of the measurement is in BD.

400 W area, whereas the 1 kW area is represented by 213 ± 13 HV0.05 on average. Crossing the transition from the 400 W area into the 1 kW area, a sharp drop in the surface hardness values can be observed.

3.3. Residual Stress Distributions

In **Figure 9**, the residual stress depth profiles for different stages (stage 1: specimen on baseplate, stage 2: specimen off baseplate, and stage 3: specimen cut) in the specimen handling process are shown. The three different specimen geometries are depicted, with the red dot pinpointing the measurement position as an example for the 1 kW area in area B. In the 400 W area along BD, tensile residual stresses are determined (cf. **Figure 9b** top). An in-depth residual stress gradient from the surface to a depth of about 1 mm can be observed for the stage 1 specimen, ranging from 600 to 100 MPa. For the stage 3 specimen, an in-depth gradient from 400 MPa to about 30 MPa is determined. Near the surface, the residual stresses are highest in stage 1. This changes below a depth of about 0.12 mm, where the residual stresses in stage 2 are slightly higher than for the other two specimens (by about 50 to 100 MPa). The difference in the residual stresses between the three stages is mostly about 100 MPa (or even less), except near the surface, where the difference is about 200 MPa. Compared to the residual stresses along BD, the in-depth gradient along TD is less steep. Tensile residual stresses are determined along TD in both stage 1 and stage 2, with higher tensile residual stresses between around 100 and 300 MPa in stage 1 compared to stage 2 with around 20–100 MPa. In stage 3, compressive residual stresses of around -100 MPa are determined near the surface and an almost stress-free state at depths greater than 0.2 mm is seen. The determined residual stresses are therefore lower than along BD except for stage 1 at depths greater than about 0.58 mm.

In the 1 kW area (cf. **Figure 9c**), tensile residual stresses are also present along BD. In both stage 1 and stage 3, the gradient

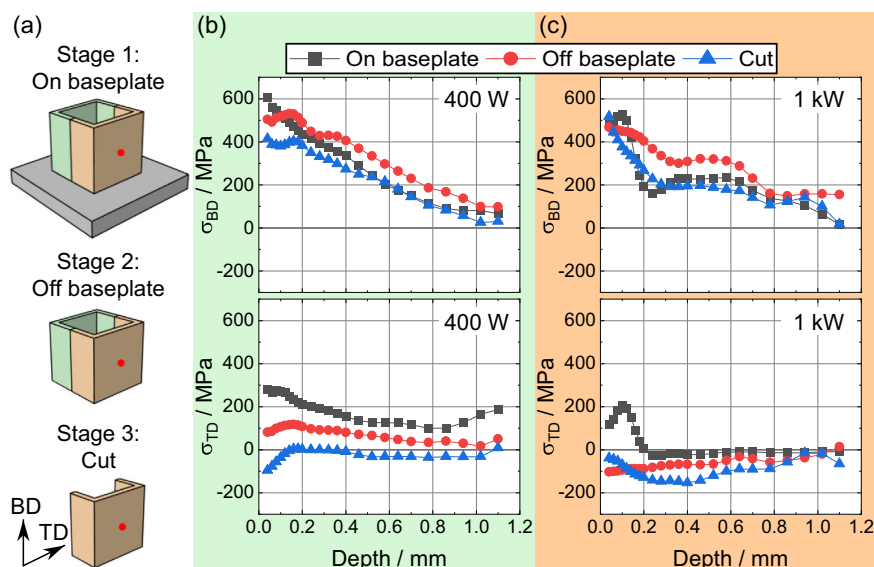


Figure 9. Residual stress depth profiles at different handling stages, i.e. for the rectangular tube profile still attached to the base plate (stage 1), after removing it from the base plate (stage 2) and after cutting the tube profile in half (stage 3), separating the 400 W from the 1 kW area: a) specimen geometries, b) residual stress depth profile along BD (top) and TD (bottom) in the 400 W area A, and c) residual stress depth profile along BD (top) and TD (bottom) in the 1 kW area B.

is much steeper within the first 0.2 mm with the residual stresses decreasing from around 500 MPa toward around 200 MPa (stage 1) or 300 MPa (stage 3). At depths below 0.2 mm, the gradient is significantly less steep with residual stresses decreasing to an almost stress-free state for depths below about 1.1 mm. The in-depth gradient in stage 2 in distinct sections is almost constant over depth with the residual stress values decreasing from around 480 MPa near the surface toward 150 MPa at a depth of about 1.1 mm. Compared to the 400 W area, the residual stress level is about the same near the surface at around 500 MPa and at a depth of about 1.0 mm with values around 100 to 150 MPa. However, due to the steeper gradient near the surface in both stage 1 and stage 3, the residual stress level between about 0.1 and 0.5 mm is around 150 to 200 MPa lower than in the 400 W area. Along TD in stage 1, tensile residual stresses with a maximum of around 200 MPa are determined up to a depth of around 0.2 mm with an almost stress-free state at higher depths. In both stage 2 and stage 3, compressive residual stresses are present in the range of around -150 to -200 MPa, with absolute values decreasing at higher depths.

The measurement positions of the five different measurements within areas A and B of the cut-open stage 3 are shown schematically in Figure 10a. In the 400 W area (Figure 10b) along BD, tensile residual stresses are determined for all five positions. In position 3, in the center of the side, an in-depth gradient from around 400 MPa near the surface to around 50 MPa at a depth of about 1.1 mm can be seen. The residual stress depth profiles in the other four measurement positions show only a slight gradient with residual stresses decreasing from between 300 and 400 MPa to around 200–300 MPa. Furthermore, the residual stresses are almost constant up to a depth of around 0.6 mm. The difference in residual stress level between the individual positions is within around 100 MPa. Along TD for positions 2,

4, and 5, tensile residual stresses are determined at around 50–100 MPa, increasing to around 150–200 MPa in depth. The residual stress level along TD is therefore lower by around 300 MPa near the surface and around 100 MPa at greater depths compared to those along BD. In contrast, compressive residual stresses of around -100 to -150 MPa are found at positions 1 and 3 near the surface, decreasing to a depth of around 0.2 mm and remaining constant within ± 50 MPa at higher depths.

Similarly, in the 1 kW area (see Figure 10c), also tensile residual stresses prevail along BD. Position 3 in the center again shows a steeper overall in-depth gradient than the other positions. Within the first 0.2 mm, at positions 1, 2, 3, and 4, a more pronounced in-depth gradient is determined, with the tensile residual stresses decreasing by around 250 MPa. At the same time, residual stresses at position 5 are almost constant. Overall differences between individual positions are mostly within 200 MPa and are therefore more pronounced than in the 400 W area. Near the surface, the tensile residual stresses at positions 2, 3, and 4 are around 100 MPa higher than in the 400 W area. Along TD, the residual stresses are around 300 MPa lower compared to those along BD. While the residual stress depth profiles at the positions 1 and 2 show compressive residual stresses around -50 MPa at higher depths, tensile residual stresses are determined at positions 4 and 5. In the center of the side, at position 3, with around -150 MPa, the highest compressive residual stresses are determined.

4. Discussion

4.1. Microstructure and Crystallographic Texture

The present study investigates microstructurally graded 316L rectangular tube profiles, which were successfully manufactured

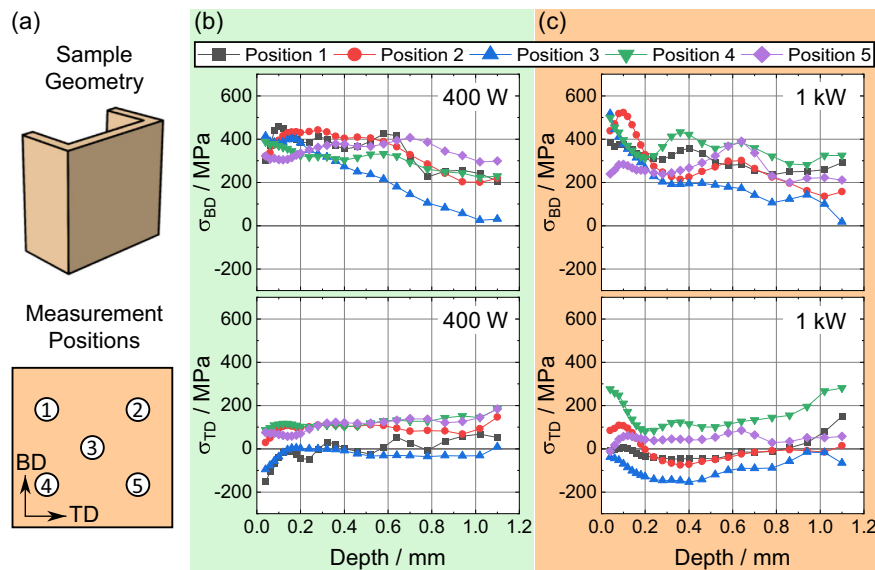


Figure 10. Residual stress distributions over the sides A and B: a) specimen geometry and measurement positions, b) residual stress depth profiles along BD (top) and TD (bottom) in the 400 W area A, and c) residual stress depth profiles along BD (top) and TD (bottom) in the 1 kW area B.

by utilizing a dual-laser system for PBF–LB/M processing. Two lasers, different in laser beam profile and maximum laser power, can be effectively used to tailor microstructural features such as grain morphology and texture (cf. Figure 3 and 4).^[38,45] Microstructure analysis of the graded specimens by EBSD revealed relatively fine and equiaxed grains with a sickle-shaped grain structure in the 400 W area compared to coarse and columnar grains, which are elongated along BD, for the 1 kW area (cf. Figure 3). Wider and shallower melt pools, influencing grain morphology and texture, are formed in the build process, pinpointing a conduction mode regime for the 1 kW laser.^[54] Considering the very low hatch distance of 50 μm in relation to the beam diameter of 1 mm for the 1 kW area, each scan track is theoretically directly exposed to the laser beam at least 21 times compared to only 1.67 times for the 400 W area (where the hatch distance was set to 120 μm with a beam diameter of 80 μm). This multiple remelting of the material induces an inherent preheating in the direct vicinity of the melt pool and, hence, reduces the cooling rate of the melt and the thermal gradient, eventually resulting in coarser grains.^[15] Nevertheless, it is noteworthy that the comparison of multiple laser exposition can only serve as a rough indicator, since process parameters, such as scanning velocity and scan track length, additionally influence the return time of the laser and hence the thermal cycling. In the following, all these influencing parameters are summarized by the term energy density. Accordingly, the growth of coarse grain in the 1 kW area is supported by the high applied volume energy of 450 Jmm^{-3} , due to the very low hatch distance and high laser power. As said before, these process conditions reduce the cooling rate and, eventually, provide more time for grain growth.^[7] Conversely, the narrow Gaussian beam profile of the 400 W laser promotes melting in the transition mode (i.e., neither conduction nor key-hole mode according to^[55]), leading to deeper melt pools and higher penetration depths. However, due to a low melt pool volume to solid material volume relation, solidification rates

up to 10^7 K s^{-1} arise and, eventually, promote the evolution of a fine-grained morphology.^[56,57]

Figure 3c presents a checkerboard morphology for the 400 W area (on the bottom surface), which is due to the 90° hatch scan rotation applied layer by layer. As expected, grain growth follows the vector of the thermal gradient. In general, the direction of the thermal gradient is perpendicular to the melt pool border and, thus, influenced by a variation of the hatch distance.^[15,58] Pronounced overlapping of the melt pools within the 1 kW area leads to an overall almost parallel heat flux along BD, eventually resulting in columnar and epitaxial grain growth. Moreover, the combination of a parallel thermal gradient with extremely dominant heat flux along BD^[58] and the prevailing low cooling rates promotes crystallographic texture evolution in $\langle 001 \rangle$ -direction with respect to BD for the 1 kW area (cf. Figure 4), which is typically observed for metals with a cubic crystal structure, as $\langle 001 \rangle$ represents the energetically favorable solidification orientation.^[7,22,25,38] Furthermore, comprehensive texture analysis at different depths from the surface reveals a pronounced crystallographic texture in higher depths within the 1 kW area. A distinct cube texture is seen at a depth of about 600 μm . Besides the 200 μm shell layer processed by the 400 W laser, the distinct cube texture has developed between a distance of 200 μm and 400 μm from the onset of the area processed by the 1 kW laser. At the interface between the 400 W and the 1 kW area in area C, a transition zone ($\approx 200 \mu\text{m}$) with heterogeneous grain morphology and weak texture is observed (cf. Figure 3), which is also reported in ref. [10]. The shell layer and this transition zone therefore shift the onset of the distinct cube texture to higher depths. The slight deviation from the ideal cube texture, most obviously seen in a depth of about 1000 μm , is thought to be caused by a limited number of grains being present in the probed volume. Using XRD to determine the integral crystallographic texture, the probed volume is larger than in the case of EBSD analysis; however, the large grain size might still limit the

number of grains contributing to the received diffraction information. In contrast to the 1 kW area, the 400 W area provokes rather globular, equiaxed grain growth due to a radial expanding heat flux. The crystallographic texture at depths higher than 400 μm is in good agreement with the crystallographic texture reported by numerous authors.^[59–62] They report on a (001)-crystallographic texture alongside the scan direction (following the thermal gradient) and a $\langle 110 \rangle$ -texture with respect to BD. Texture measurements presented in the present study revealed a Goss texture, which can be rationalized by the hatch scan rotation at an $\pm 45^\circ$ angle to ND (cf. section 2). Moreover, a gradient of the crystallographic texture is seen in the case of the 400 W area from the surface toward higher depths as well, which is characterized by a less pronounced texture and smaller grains near the surface.

Generally, PBF-LB/M processed parts exceed the cooling rates of conventional manufacturing techniques and typically vary in the range of 10^4 – 10^7 K s^{-1} , thus promoting the evolution of unique microstructures.^[11,15,22,56,57] A typical cellular, substructure network, which is frequently described for PBF-LB/M manufactured 316L, was likewise shown in the present study in the SE-contrast micrographs (cf. Figure 5c,d). The substructures are enriched in microsegregations of alloying elements such as Mo and Cr, as can be derived from the EDS mappings shown in Figure 6c,e. Such characteristics are in line with observations in numerous previous studies.^[6,11,22] The appearance of the substructures is altered depending on process parameters and melt pool characteristics, respectively, due to partially changing Marangoni convection modes, which are affected by temperature and surface tension gradients.^[22] Figure 5c visualizes the relation between substructure morphology and melt pool appearance. Here, it can be seen that a melt pool boundary crosses a strip-like cellular network in the 400 W area. Nevertheless, direct comparison of the IPF map in Figure 5a and the corresponding SEM image in Figure 5c shows as well a transition of the subgrain morphology within a grain, which is not crossed by a melt pool boundary. The difference in magnitude of 0.49–1.20 μm between the substructures in the 400 W and 1 kW areas is obvious. Larger substructures are seen for the condition being characterized by larger grains. The observation is in line with the difference in cooling rates between the 400 W and 1 kW area. An estimation for the cooling rates can be elaborated by the evaluation of dendrite arm spacing as proposed in literature, for example, in refs. [13–15]. Application of this approach (to the sizes of the substructures here) pinpoints a factor of 2.45 increased cooling rate for the 400 W area compared to the 1 kW area.

4.2. Mechanical Properties

Considering the stress–strain curves displayed in Figure 7, clearly differing mechanical responses are seen within the 400 W and 1 kW specimens. Generally, $R_{p0.2}$ values for both areas (i.e., 424 MPa and 516 MPa for the 400 W and 1 kW specimens, respectively) are superior to conventionally processed wrought and cast counterparts, which is in line with findings reported in the literature on PBF-LB/M processed 316L.^[7,8,34–36] Planar dislocation slip was found to be the dominant deformation mechanism in PBF-LB/M processed 316L.^[25]

Hence, strengthening is enabled through impeding dislocation motion in mechanically loaded parts. The well-known Hall–Petch relation describes the contribution of grain boundaries to strengthening.^[63–65] However, applying the Hall–Petch equation with the information on grain size for both the 400 W and 1 kW area (cf. section 3) yields an insufficient, underestimated value of $R_{p0.2}$ compared to the experimentally obtained results (cf. Figure 7).^[25,66] Yang et al.^[22] as well as Zhong et al.^[11] proposed to calculate the Hall–Petch strengthening effect by taking into account the size of the substructures, eventually resulting in well-approximated yield stresses for PBF-LB/M 316L. Thus, the significant enhancement of the yield strength compared to conventionally processed parts is linked to the formation of the aforementioned unique substructures (cf. Figure 5c,d), as already predicted in literature, for example, in refs. [33,67]. The substructures enriched by microsegregation of Cr and Mo, as demonstrated by the results of the EDS measurements in Figure 6, act as barriers for dislocation movement and, thus, foster accumulation and formation of new dislocations inside the cells finally promoting severe dislocation–dislocation interaction. An estimation for $R_{p0.2}$ for the 400 W and 1 kW area taking into account the substructures (cf. section 3) leads to values of 413 MPa and 264 MPa, respectively. Referring to the substructures in the present study, it can be concluded that the smaller average cell size in the 400 W area yields a higher $R_{p0.2}$ due to the enhanced pinning effect of dislocations due to a higher volume fraction of substructures. Moreover, substructure strengthening seems to be the main mechanism contributing to the overall yield stress. Obviously, an accurate approximation still is not obtained, especially for the 1 kW area (cf. Figure 7). Accordingly, it can be concluded that $R_{p0.2}$ is a superposition of multiple strengthening mechanisms, including grain boundary and substructure strengthening, as proposed by the authors in ref. [25]. Furthermore, an orientation strengthening as a possible strengthening factor is assessed based on the Schmid factor. The maximum Schmid factors are determined based on the crystallographic texture at 2 mm depth and found to be 0.495 and 0.445 for the 400 W and 1 kW areas A and B, respectively. This implies a slightly higher orientation strengthening contribution to the overall strength for the 1 kW area, due to higher resistance against planar slip. Upon exceeding $R_{p0.2}$, the formation of new dislocation occurs. Consequently, those strengthening mechanisms are also reflected in the UTS through dislocation–dislocation interaction, resulting in a higher value of 618 MPa for the 400 W area, compared to the 1 kW area with 542 MPa. The coarser substructures of the 1 kW area are associated with a lower dislocation density inside the cells. Therefore, more intense formation of new dislocations during mechanical loading is thought to result in a slightly higher work hardening capability compared to the 400 W area. This is confirmed by experimental data through the relation of $R_{p0.2}$ to UTS (cf. section 3). Despite superior strengths compared to conventionally manufactured parts of 316L, high EF for both the 400 W and the 1 kW area are maintained (cf. Figure 7). This already has been numerous reported for PBF-LB/M 316L.^[22,24,25,33,37] High ductility is thought to be retained due to a homogeneous deformation without severe local stress concentration, emanating from the substructures, similar to findings reported for ultrafine-grained and nanocrystalline materials.^[68,69] Moreover,

twinning-induced plasticity (TWIP) and transformation-induced plasticity (TRIP), which are dependent on the (local) chemical composition, are reported as potential mechanisms promoting the increase of ductility.^[24,25,37] Besides differences regarding the impact of the size of the substructures on the quasi-static mechanical properties, crystallographic texture is another crucial factor to be considered. Differing YM values between the 400 W and 1 kW area result from the elastic anisotropy in FCC lattices, owing to the lowest YM in $\langle 001 \rangle$ -direction and the highest in $\langle 111 \rangle$ -direction.^[70] The lower YM for the 1 kW area can be rationalized by the pronounced crystallographic texture with a $\langle 001 \rangle$ -orientation in BD. The experimentally determined macroscopic YM of 145 GPa is in good agreement with the calculated YM of 143 GPa, deduced from MTEX calculation, based on the crystallographic texture at 2 mm depth. The higher macroscopic YM for the 400 W area of 173 GPa is a result of the preferred crystallographic $\langle 110 \rangle$ texture, and again matches well the MTEX calculated YM of 176 GPa. Similar results were presented in a former work of Niendorf et al.^[38] revealing a comparable low YM of 115 GPa for specimens processed with a high-energy top-hat laser beam in PBF-L/M 316L.

The presented Vickers hardness map in Figure 8 illustrates the hardness distribution within the ND-TD plane for the microstructural interface of a graded PBF-L/M processed 316L specimen. It can be seen that the microstructural gradation is influence through the aforementioned strengthening mechanisms. The larger grain size, in combination with coarser substructures of the 1 kW area (cf. Figure 3 and 5), results in a lower hardness. In contrast, the 400 W area exhibits higher hardness due to finer grains and finer cellular substructure sizes. Additionally, the pronounced gradient in crystallographic texture influences the hardness measurement. Reduced hardness values were already reported for indentation along the $\langle 001 \rangle$ -direction of FCC 316L material, whereas maximum hardness was found for the $\langle 111 \rangle$ -direction.^[70] The 1 kW area exhibits a pronounced $\langle 001 \rangle$ -texture, which is therefore additionally superimposing the softening effect being rationalized by the coarse grain structure. In summary, it is revealed that not only the microstructural morphology sharply changes upon crossing the interface from 400 W to 1 kW area, but also the mechanical properties in case of hardness. It needs to be noted at this point that the higher hardness surrounding the softer 1 kW area reflects the shell of the material processed by the 400 W laser.

4.3. Residual Stress Distribution

The residual stress depth profiles generally show higher tensile residual stresses near the surface along BD with an in-depth gradient toward the center of the specimen. This is expected and was already detailed in other studies^[71] where also higher tensile residual stresses near the surface and compressive residual stresses in the center of the structures (to balance the tensile residual stresses in order to achieve equilibrium) were determined. According to refs. [44,72], the highest residual stresses are located at the onset of the scan tracks, which coincide with the surface of the specimens studied. Hence, an in-depth gradient determined for both the 400 W and the 1 kW area is seen in the present study. The steep in-depth gradient within the first

200 μm in the 1 kW area is attributed to the shell layer being processed using the 400 W laser. When processing the core area using the 1 kW laser, the inner parts of the shell layer get melted again. Similar to overlapping scan paths in the hatching areas, already solidified areas are remolten, eventually leading to a decrease in the residual stress values.^[73]

Removing the specimens from the baseplate, as well as cutting them open, does not promote significant elastic redistribution of the residual stress component along BD. This is attributed to the still-existing geometric constraints along this direction. On the contrary, cutting the specimen open allows for relaxation along TD due to the removal of the geometric constraints. In case of the 400 W area exhibiting tensile residual stresses, this elastic redistribution of residual stresses leads to an almost stress-free state along TD within the probed volume (assessed using the incremental hole drilling method). In the case of the 1 kW area, which is already stress-free along TD in as-built condition on the baseplate, cutting leads to minor compressive residual stresses within the probed volume. These compressive residual stresses are in equilibrium with the inner volumes of the specimens also showing low compressive residual stress values along TD after cutting. Since measurements on the inside can only be done considering the cut-open state, these results are not further discussed here. Lower residual stresses along TD than BD were also reported in literature, for example, by ref. [74].

The lateral residual stress distribution over a side of the rectangular tubes shows a difference between the center of the sides and the corners. While in the center a more distinct in-depth gradient is present, near the edges this gradient is less pronounced. Wu et al.^[71] found similar results in an L-shaped bracket, where the in-depth gradient was steeper at a larger distance to the corner than next to it. In both the 400 W and the 1 kW area, the measurements in the corners show a similar trend. No distinct difference, for example, along BD, can be found. This is in contrast to refs. [44,75], where authors reported that the residual stresses change along BD. However, since in the present study positions 1 and 2 are ≈ 10 mm away from the top layer and positions 4 and 5 ≈ 10 mm away from the baseplate, the influences of the first and last layers are not assessed. While the residual stresses are dependent on the complex interplay of many influencing factors and, eventually, a highly localized phenomenon, already minor changes in boundary conditions can lead to possible deviations of the overall residual stress distribution in the 400 W and the 1 kW areas. Still, findings reported here point at rather homogeneous stress fields, as revealed by similar trends and residual stress levels for all four corners considered. The larger scattering range within the 1 kW area is thought to be caused by the rather large grain size.

5. Conclusion

In the present study, rectangular tube profiles of 316L were processed via PBF-LB/M. Particular attention is given to microstructural gradation of grain size and crystallographic texture by applying a dual-laser system, equipped with a 1 kW top-hat and a 400 W Gaussian intensity profile laser, respectively. Volumes processed using these different lasers are characterized by differing volume energy densities and distinctive beam

diameters. For all specimens, microstructure, crystallographic texture, mechanical behavior as well as residual stress states were investigated. From the results presented, the following conclusions can be drawn: 1) The 1 kW laser, operating with a wider beam diameter in conduction mode and a low hatch distance, promotes the evolution of a coarse-grained microstructure with pronounced (001)-crystallographic texture along BD, rationalized by relatively low cooling rates and strongly directed thermal gradients. Conversely, the 400 W laser, utilizing a narrow beam and operating in transition mode, resulted in finer grains with equiaxed morphology rationalized by relatively high cooling rates and more diffuse heat flux. Moreover, a distinct interface concerning the microstructure between 400 W and 1 kW area was achieved. 2) Within the 400 W area, a primary Goss texture is revealed by XRD analysis at a depth of 400 μm . The 1 kW area instead exhibits a more pronounced cube texture, which is very obvious at a depth of 600 μm . In both areas, an in-depth gradient of crystallographic texture is found and rationalized through locally differing process parameters and cooling conditions. 3) The unique substructures, enriched with Cr and Mo segregations as revealed by EDS analysis, act as a dislocation barrier, contributing to the superior mechanical performance of both microstructural conditions (compared to conventionally processed 316L). Substructure analysis by applying the dendrite arm spacing approach, revealed a significant influence of cooling rates on the cellular substructure morphology and size. Cell sizes are found to be 0.49 μm and 1.20 μm for the 400 W and 1 kW area, respectively, implying an increased cooling rate by the factor of 2.45 for the 400 W area compared to the 1 kW area. 4) Mechanical properties, i.e., hardness and tensile strength, reflected the combined effects of grain morphology, substructure characteristics, and crystallographic texture. The 400 W area exhibited higher hardness and strength due to finer grains, smaller substructures, and most effective dislocation pinning effects. In contrast, the 1 kW area, characterized by coarser grains, larger substructures, and pronounced (001)-texture, exhibited lower yield strength and UTS but slightly enhanced work-hardening behavior. 5) Residual stress distributions were characterized through the incremental hole drilling method. In both areas, i.e., in the 400 W and the 1 kW area, higher tensile residual stresses are determined along BD than along TD. Both are characterized by a pronounced gradient from the surface toward the center of the specimen within the probed volume. Upon cutting the component from the baseplate, and upon further cutting the tube profiles, a rearrangement of the residual stress distribution is seen. The effect is most pronounced for the 400 W area for the residual stress component in TD, i.e., the component parallel to the base plate. 6) The residual stress distribution over one side is relatively homogeneous, although slightly more pronounced scattering is seen in the 1 kW area. Such characteristics can be attributed to the large grains prevailing in the 1 kW area.

Acknowledgements

The authors gratefully acknowledge funding by “Deutsche Forschungsgemeinschaft” (DFG), grant no. 505457585. This work was embedded in the project BitWerk funded by the University of Kassel.

Open Access funding enabled and organized by Projekt DEAL.

Conflict of Interest

The authors declare no conflict of interest.

Author Contributions

Nico Möller: conceptualization (equal); data curation (equal); formal analysis (equal); investigation (equal); methodology (equal); validation (equal); visualization (equal); writing—original draft preparation (equal); writing—review and editing (equal). **Florian Loebich:** conceptualization (equal); data curation (equal); formal analysis (equal); investigation (equal); methodology (equal); validation (equal); visualization (equal); writing—original draft preparation (equal); writing—review and editing (equal). **Thomas Wegener:** conceptualization (equal); investigation (equal); methodology (equal); writing—review and editing (equal). **Julia Richter:** conceptualization (equal); investigation (equal); methodology (equal); writing—review and editing (equal). **Jens Gibmeier:** funding acquisition (equal); supervision (equal); conceptualization (equal); writing—review and editing (equal). **Thomas Niendorf:** funding acquisition (equal); supervision (equal); writing—review and editing (equal).

Data Availability Statement

The data that support the findings of this study are available from the corresponding author upon reasonable request.

Keywords

crystallographic texture, microstructure gradient, PBF-LB/M 316L, residual stress, substructure

Received: February 11, 2025

Revised: March 31, 2025

Published online:

- [1] D. Herzog, V. Seyda, E. Wycisk, C. Emmelmann, *Acta Mater.* **2016**, 117, 371.
- [2] T. DebRoy, H. L. Wei, J. S. Zuback, T. Mukherjee, J. W. Elmer, J. O. Milewski, A. M. Beese, A. Wilson-Heid, A. De, W. Zhang, *Prog. Mater. Sci.* **2018**, 92, 112.
- [3] S. Chowdhury, N. Yadaiah, C. Prakash, S. Ramakrishna, S. Dixit, L. R. Gupta, D. Buddhi, *J. Mater. Res. Technol.* **2022**, 20, 2109.
- [4] Stainless Steel 316L - 1.4404 Data Sheet - thyssenkrupp Materials (UK). <https://www.thyssenkrupp-materials.co.uk/stainless-steel-316l-14404.html> (accessed: November 2024).
- [5] T. Kurzynowski, K. Gruber, W. Stopyra, B. Kuźnicka, E. Chlebus, *Mater. Sci. Eng.: A* **2018**, 718, 64.
- [6] M. L. Montero Sistiaga, S. Nardone, C. Hautfenne, J. Van Humbeeck, *Effect of Heat Treatment Of 316L Stainless Steel Produced by Selective Laser Melting (SLM)* **2016**.
- [7] Č. Donik, J. Kraner, I. Paulin, M. Godec, *Metals* **2020**, 10, 919.
- [8] I. Tolosa, F. Garciandía, F. Zubiri, F. Zapirain, A. Esnaola, *Int. J. Adv. Manuf. Technol.* **2010**, 51, 639.
- [9] N. Ahmed, I. Barsoum, G. Haidemenopoulos, R. A. Al-Rub, *J. Manuf. Process.* **2022**, 75, 415.
- [10] F. Brenne, T. Niendorf, *Mater. Sci. Eng.: A* **2019**, 764, 138186.
- [11] Y. Zhong, L. Liu, S. Wikman, D. Cui, Z. Shen, *J. Nucl. Mater.* **2016**, 470, 170.
- [12] S. Chandra, C. Wang, S. B. Tor, U. Ramamurty, X. Tan, *Nat. commun.* **2024**, 15, 3094.
- [13] T. F. Bower, *Trans. Metall. Soc. AIME* **1966**, 236, 624.

- [14] A. M. Mullis, L. Farrell, R. F. Cochrane, N. J. Adkins, *Metall. Mater. Trans. B* **2013**, 44, 992.
- [15] A. Iveković, M. L. Montero-Sistiaga, J. Vleugels, J.-P. Kruth, K. Vanmeensel, *J. Alloys Compd.* **2021**, 864, 158803.
- [16] IMOA International Molybdenum Association, Molybdenum properties, <https://www.imoa.info/molybdenum/molybdenum-properties.php> (accessed: December 2024).
- [17] D. J. Maykuth, A. Gilbert, Defense Metals Information Center, United States. Office of the Director of Defense Research, Engineering, United States. Air Force. Systems Command. Research, Technology Division, Chromium and Chromium Alloys, Defense Metals Information Center, Battelle Memorial Institute **1966**.
- [18] Di Wang, C. Song, Y. Yang, Y. Bai, *Mater. Des.* **2016**, 100, 291.
- [19] E. F. Özel, D. Pedre, C. Müller, Y. Thomann, R. Thomann, H. Mozaffari-Jovein, *J. Exp. Theor. Anal.* **2023**, 1, 64.
- [20] R. E. Smallman, A. Ngan, *Solidification, In Modern Physical Metallurgy*, Elsevier, Oxford, UK **2014**, pp. 93–119.
- [21] D. M. Stefanescu, R. Ruxanda, *Fundamentals of Solidification, in Metallography and Microstructures* (Ed: G.F. Vander Voort), ASM International, Metals Park, Ohio, US **2004**, pp. 71–92.
- [22] X. Yang, W. Ma, Y. Ren, S. Liu, Y. Wang, W. Wang, H. Tang, *J. Iron Steel Res. Int.* **2021**, 28, 1159.
- [23] F. Svahn, P. Mishra, E. Edin, P. Åkerfeldt, M.-L. Antti, *J. Mater. Res. Technol.* **2024**, 28, 1452.
- [24] Y. M. Wang, T. Voisin, J. T. McKeown, J. Ye, N. P. Calta, Z. Li, Z. Zeng, Y. Zhang, W. Chen, T. T. Roehling, R. T. Ott, M. K. Santala, P. J. Depond, M. J. Matthews, A. V. Hamza, T. Zhu, *Nat. Mater.* **2018**, 17, 63.
- [25] Z. Zhou, J. Lv, M. Gui, W. Yang, *Int. J. Plast.* **2024**, 178, 104008.
- [26] T. Voisin, J.-B. Forien, A. Perron, S. Aubry, N. Bertin, A. Samanta, A. Baker, Y. M. Wang, *Acta Mater.* **2021**, 203, 116476.
- [27] C. Li, Z. Y. Liu, X. Y. Fang, Y. B. Guo, *Procedia CIRP* **2018**, 71, 348.
- [28] S. Santa-aho, M. Kiviluoma, T. Jokiaho, T. Gundgire, M. Honkanen, M. Lindgren, M. Vippola, *Metals* **2021**, 11, 182.
- [29] T. Ge, Y. Li, D. Gao, C. Yang, F. Li, *J. Manuf. Process.* **2024**, 124, 345.
- [30] S. An, D.-R. Eo, H. Lim, I. Sohn, K. Choi, *Addit. Manuf.* **2024**, 91, 104339.
- [31] B. Zhang, Y. Li, Q. Bai, *Chin. J. Mech. Eng.* **2017**, 30, 515.
- [32] W.-J. Lai, A. Ojha, Z. Li, C. Engler-Pinto, X. Su, *Prog. Addit. Manuf.* **2021**, 6, 375.
- [33] A. Riemer, S. Leuders, M. Thöne, H. A. Richard, T. Tröster, T. Niendorf, *Eng. Fract. Mech.* **2014**, 120, 15.
- [34] T. M. Mower, M. J. Long, *Mater. Sci. Eng.: A* **2016**, 651, 198.
- [35] F. Bartolomeu, M. Buciumeanu, E. Pinto, N. Alves, O. Carvalho, F. S. Silva, G. Miranda, *Addit. Manuf.* **2017**, 16, 81.
- [36] R. Casati, J. Lemke, M. Vedani, *J. Mater. Sci. Technol.* **2016**, 32, 738.
- [37] Y. J. Yin, J. Q. Sun, J. Guo, X. F. Kan, D. C. Yang, *Mater. Sci. Eng.: A* **2019**, 744, 773.
- [38] T. Niendorf, S. Leuders, A. Riemer, F. Brenne, T. Tröster, H. A. Richard, D. Schwarze, *Adv. Eng. Mater.* **2014**, 16, 857.
- [39] E. C. Aifantis, *Int. J. Plast.* **1987**, 3, 211.
- [40] D. Kuhlmann-Wilsdorf, *Mater. Sci. Eng.: A* **1989**, 113, 1.
- [41] C. Bean, F. Wang, M. A. Charpagne, P. Villechaise, V. Valle, S. R. Agnew, D. S. Gianola, T. M. Pollock, J. C. Stinville, *Int. J. Plast.* **2022**, 159, 103436.
- [42] D. Kumar, G. Shankar, K. G. Prashanth, S. Suwas, *J. Alloys Compd.* **2024**, 976, 173040.
- [43] T. Niendorf, S. Leuders, A. Riemer, H. A. Richard, T. Tröster, D. Schwarze, *Metall. Mater. Trans. B* **2013**, 44, 794.
- [44] J. C. Stinville, C. Tromas, P. Villechaise, C. Templier, *Scr. Mater.* **2011**, 64, 37.
- [45] T. Niendorf, F. Brenne, M. Schaper, A. Riemer, S. Leuders, W. Reimche, D. Schwarze, H. J. Maier, *Rapid Prototyp. J.* **2016**, 22, 630.
- [46] J. Schindelin, I. Arganda-Carreras, E. Frise, V. Kaynig, M. Longair, T. Pietzsch, S. Preibisch, C. Rueden, S. Saalfeld, B. Schmid, J.-Y. Tinevez, D. J. White, V. Hartenstein, K. Eliceiri, P. Tomancak, A. Cardona, *Nat. Methods* **2012**, 9, 676.
- [47] F. Bachmann, R. Hielscher, H. Schaebe, *Solid State Phenom.* **2010**, 160, 63.
- [48] ASTM E837-20, Standard Test Method for Determining Residual Stresses by the Hole-Drilling Strain-Gage Method. Standard Test Method E837-20 **2022**, i, 1–16.
- [49] T. Schwarz, H. Kockelmann, *Messtechnische Briefe* **1993**, 29, 33.
- [50] S. Schuster, J. Gibmeier, *Exp. Mech.* **2016**, 56, 369.
- [51] N. Simon, T. Mrotzek, J. Gibmeier, *Mater. Perform. Charact.* **2018**, 7, 409.
- [52] E. Held, S. Schuster, J. Gibmeier, *Adv. Mater. Res.* **2014**, 996, 283.
- [53] H. M. Ledbetter, *Br. J. Non-Destructive Test.* **1981**, 23, 286.
- [54] C. Tenbrock, F. G. Fischer, K. Wissenbach, J. H. Schleifenbaum, P. Wagenblast, W. Meiners, J. Wagner, *J. Mater. Process. Technol.* **2020**, 278, 116514.
- [55] S. Patel, M. Vlasea, *Materialia* **2020**, 9, 100591.
- [56] L. Thijs, M. L. Montero Sistiaga, R. Wauthle, Q. Xie, J.-P. Kruth, J. van Humbeeck, *Acta Mater.* **2013**, 61, 4657.
- [57] M. H. Farshidianfar, A. Khajepour, A. P. Gerlich, *J. Mater. Process. Technol.* **2016**, 231, 468.
- [58] S. Kou, *JOM* **2003**, 55, 37.
- [59] L. Thijs, K. Kempen, J. P. Kruth, J. van Humbeeck, *Acta Mater.* **2013**, 61, 1809.
- [60] J. J. Marattukalam, D. Karlsson, V. Pacheco, P. Beran, U. Wiklund, U. Jansson, B. Hjörvarsson, M. Sahlberg, *Mater. Des.* **2020**, 193, 108852.
- [61] K. A. Sofinowski, S. Raman, X. Wang, B. Gaskey, M. Seita, *Addit. Manuf.* **2021**, 38, 101809.
- [62] O. Andreau, I. Koutiri, P. Peyre, J. D. Penot, N. Saintier, Pessar, E. d, De T, T. erris, C. Dupuy, T. Baudin, *J. Mater. Process. Technol.* **2019**, 264, 21.
- [63] E. O. Hall, *Proc. Phys. Soc. B* **1951**, 64, 747.
- [64] R. B. Figueiredo, M. Kawasaki, T. G. Langdon, *Prog. Mater. Sci.* **2023**, 137, 101131.
- [65] N. J. Petch, *J. Iron Steel Inst.* **1953**, 174, 25.
- [66] X. H. Chen, J. Lu, L. Lu, K. Lu, *Scr. Mater.* **2005**, 52, 1039.
- [67] T. Niendorf, F. Brenne, *Mater. Charact.* **2013**, 85, 57.
- [68] T. Niendorf, D. Canadinc, H. J. Maier, I. Karaman, S. G. Sutter, *Int. J. Mater. Res.* **2006**, 97, 1328.
- [69] D. Canadinc, E. Biyikli, T. Niendorf, H. J. Maier, *Adv. Eng. Mater.* **2011**, 13, 281.
- [70] A. S. Wu, D. W. Brown, M. Kumar, G. F. Gallegos, W. E. King, *Metall. Mater. Trans. A: Phys. Metall. Mater. Sci.* **2014**, 45, 6260.
- [71] Y. Liu, Y. Yang, Di Wang, *Int. J. Adv. Manuf. Technol.* **2016**, 87, 647.
- [72] Di Wang, S. Wu, Y. Yang, W. Dou, S. Deng, Z. Wang, S. Li, *Materials* **2018**, 11, 1821.
- [73] C. Chen, J. Yin, H. Zhu, Z. Xiao, L. Zhang, X. Zeng, *Int. J. Mach. Tools Manuf.* **2019**, 145, 103433.
- [74] C. H. Yu, R. L. Peng, V. Luzin, M. Sprengel, M. Calmunger, J. E. Lundgren, H. Brodin, A. Kromm, J. Moverare, *Addit. Manuf.* **2020**, 36, 101672.
- [75] J. Ding, P. Colegrove, J. Mehnen, S. Ganguly, P. M. Almeida, F. Wang, S. Williams, *Comput. Mater. Sci.* **2011**, 50, 3315.
- [76] Specification for Stainless Steel Bars and Shapes, A01 Committee, West Conshohocken, PA.
- [77] DIN EN 10088-1:2024-04, Nichtrostende Stähle_- Teil_1: Verzeichnis der nichtrostenden Stähle; Deutsche Fassung EN_10088-1:2023, Berlin.